RSC Advances

ROYAL SOCIETY OF CHEMISTRY

www.rsc.org/advances

Photo-reduction assisted synthesis of MnO_2/reduced graphene oxide/P25 for electrochemical detection of hydrogen peroxide

Shoufang Cui, Yu Li, Dongmei Deng[*]*, Lilan Zeng, Xiaoxia Yan, Jun Qian，*

Liqiang Luo[*]

College of Sciences, Shanghai University, Shanghai 200444, PR China

Abstract

In this work, we report the synthesis of MnO_2/RGO (reduced graphene oxide)/P25 nanocomposites for non-enzymatic hydrogen peroxide sensor. MnO_2/RGO/P25 nanocomposites were synthesized with photo-reduction approach and characterized by field emission scanning electron microscopy, X-ray photoelectron spectroscopy, Fourier transform infrared spectroscopy and Raman spectroscopy. The non-enzymatic hydrogen peroxide sensor was fabricated by dropping MnO_2/RGO/P25 nanocomposites on the surface of glassy carbon electrode. Electrochemical measurements of MnO_2/RGO/P25 modified electrode were carried out on electrochemical workstation. The as-prepared sensor exhibited high electrocatalytic activity, selectivity and stability towards the oxidation of H_2O_2. Under optimum conditions, the calibration curve for H_2O_2 determination was linear in the range from 1.0×10^{-6} to 4.0×10^{-3} M ($R^2 = 0.999$) with a detection limit of 3×10^{-7} M (S/N = 3).

Keywords: MnO_2; photo-reduction; reduced graphene oxide; P25; hydrogen peroxide

[*] Corresponding author. *E-mail addresses:* luck@shu.edu.cn (L. Luo). dmdeng@i.shu.edu.cn (D. Deng).

1. Introduction

Hydrogen peroxide is one of the most important and common oxidizing agent widely utilized in clinical area, biochemistry, pharmaceutical industry and environmental fields [1]. Therefore, accurate and fast detection of H_2O_2 via highly sensitive and cost-effective sensors is of great practical significance. Thus, many detection methods have been developed, such as titrimetry [2], chemiluminescence [3−4], fluorescence [5], spectrophotometry [6] and electrochemical method [7−9]. Among them, electrochemical method is the most attractive because of its high sensitivity, low cost and operational simplicity. Over the past decades, intensive interests have been directed to electrochemical detection of H_2O_2 based on enzymes due to their high sensitivity and selectivity [10−12]. However, the drawbacks of enzymes based sensors such as limited lifetime, instability, poor reproducibility and complicated fabrication procedures have impeded them from being prevailing [13]. In recent years, much effort has been devoted to non-enzymatic electrochemical detection of H_2O_2 to overcome these disadvantages due to the intrinsic fragility nature of enzymes [14]. Various materials have been successfully applied extensively in fabricating high efficient non-enzymatic electrochemical sensors, such as metals [15-18], alloys [19], transition metal oxide nanoparticles [20] and graphene [21−23]. In particular, as one outstanding electrocatalytic material towards H_2O_2, manganese dioxide has drawn intensive attentions in virtue of excellent physicochemical properties, low cost, environmental benignity, safe operation voltage and non-toxic [24−26].

Reduced graphene oxide (RGO) is a kind of attractive material in the scientific community owning to its excellent mobility of charge carriers, high thermal conductivity, great chemical stability, high mechanical flexibility and large specific surface area [27−29]. So far, various synthesis methods have been developed to prepare RGO such as chemical reduction, electrochemical reduction and thermal reduction methods [30−33]. In recent years, photo-reduction methods turning graphene oxide into RGO in the presence of TiO_2 and avoiding drawbacks caused by chemical reduction methods and thermal reduction methods have been developed by researchers [34]. Compared with the chemical and thermal reduction of GO, photo-reduction is a facile and green reduction method to prepare RGO.

TiO_2 is one of the most promising materials and has been well studied over the years because of its photocatalytic properties, non-toxicity, high chemical stability and huge potential application value [35−37]. When TiO_2 is irradiated with UV lights, the electrons will be excited from the valence bands to the conduction bands, leaving holes in valence bands and generating photo electron-hole pairs in this process [38]. Photogenerated electrons and holes migrate on surface of TiO_2, triggering reductive reaction and oxidative reaction, respectively. P25 is a kind of commercial TiO_2 nanoparticle consisting 80% anatase phase and 20% rutile phase. The mixed phases suppress the recombination of the photo-electrons and photo-holes, which promote its photocatalytic efficiency. Based on this, many kinds of TiO_2–RGO nanocomposites have been developed to improve the photocatalysis property of TiO_2.

In this work, we successfully synthesized MnO_2/RGO/P25 nanocomposites using photo-reduction method. MnO_2/RGO/P25 nanocomposites were characterized by Field emission scanning electron microscopy (FESEM), X-ray photoelectron spectroscopy (XPS), Fourier transform infrared (FTIR) spectroscopy and Raman spectroscopy. Cyclic voltammetry (CV) of MnO_2/RGO/P25 modified sensor were conducted on electrochemical workstation. The as-prepared sensor exhibited high electrocatalytic activity, good selectivity and stability toward the oxidation of H_2O_2. To the best of our knowledge, this is the first report on photo-reduction assisted synthesis of MnO_2/RGO/P25 nanocomposites and their use in electrochemical detection of hydrogen peroxide.

2. Experimental section

2.1 Materials and apparatus

Graphene oxide was purchased from Institute of Coal Chemistry，Chinese Academy of Sciences (Shanxi, China). The commercial TiO_2 (Degussa P25) was obtained from Degussa Co., Ltd. (Germany). $KMnO_4$, KH_2PO_4, K_2HPO_4•$3H_2O$, hydrogen peroxide (H_2O_2，30%), CH_3CH_2OH and NaOH were purchased from Sinopharm Chemical Reagent Co., Ltd. (Shanghai, China). 0.1 M phosphate buffer solutions (PBS, pH 6-10) were prepared from NaH_2PO_4, Na_2HPO_4•$3H_2O$ and NaOH and used as supporting electrolytes. All chemicals were of analytical grade. Ultra-pure water was used throughout the experiment. UV lamp (16 W) was purchased from Hangzhou Yaguang Lamp Co., Ltd. (Hangzhou, China).

The morphologies of GO, RGO/P25 and MnO_2/RGO/P25 were characterized by field emission scanning electron microscopy (Zeiss, Germany). The chemical states of elements in MnO_2/RGO/P25 were analyzed by WSCALAB 250 Xi X-ray photoelectron spectroscopy (England) using a source of Al Kα radiation with energy of 1486.6 eV. Infrared spectra of GO, RGO/P25 and MnO_2/RGO/P25 were carried out on an AVATAR 370 Fourier transform infrared spectrometer (FTIR, America) in the region of 400–4000 cm^{-1}. Raman spectra of GO, RGO/P25 and MnO_2/RGO/P25 were characterized by inVia Reflex (Renishaw, England) with an excitation laser wavelength of 514.5 nm. All electrochemical measurements were performed on a CHI660C Electrochemical Workstation (Shanghai Chenhua, China) with a conventional three-electrode system, in which a saturated calomel electrode (SCE), platinum foil and MnO_2/RGO/P25 modified GCE were served as the as reference, counter and working electrode, respectively.

2.2 Synthesis of MnO_2/RGO/P25 nanocomposites

MnO_2/RGO/P25 nanocomposites were synthetized using photo-assisted reduction method. In brief, 0.2 mg P25 was dispersed in 2 mL GO (1.0 mg/mL) solution under magnetic stirring at room temperature (25℃) and the suspension solution was vigorously stirred for 1 h under UV irradiation to obtain RGO/P25 homogenous dispersion. After that, a series of $KMnO_4$ (0.2, 0.4, 0.6, 0.8, and 1.0 mg) solutions with different amount were dropwise added into the same volume RGO/P25 homogenous dispersion solutions which had been irradiated with UV light to synthesize MnO_2/RGO/P25 nanocomposites. Finally, MnO_2/RGO/P25

nanocomposites were centrifuged and washed with ultrawater for 3 times to further analysis.

2.3 Preparation of MnO_2/RGO/P25 modified electrodes

A glassy carbon electrode (GCE, 3 mm in diameter) was polished with 0.05 μm alumina slurries using Buehler polishing kit, followed by washing with deionized water, ethanol and finally deionized water under ultrasound conditions (each for 3 min), and drying at room temperature to remove any adsorbed impurities on the electrode surface. 5 μL of as-prepared MnO_2/RGO/P25 nanocomposites was dropped onto the surface of GCE and dried in air under the infrared lamp for 15 min. For comparison, 5 μL of GO and RGO/P25 were dropped onto GCE and dried at the same conditions as MnO_2/RGO/P25-GCE to obtain GO-GCE and RGO/P25-GCE.

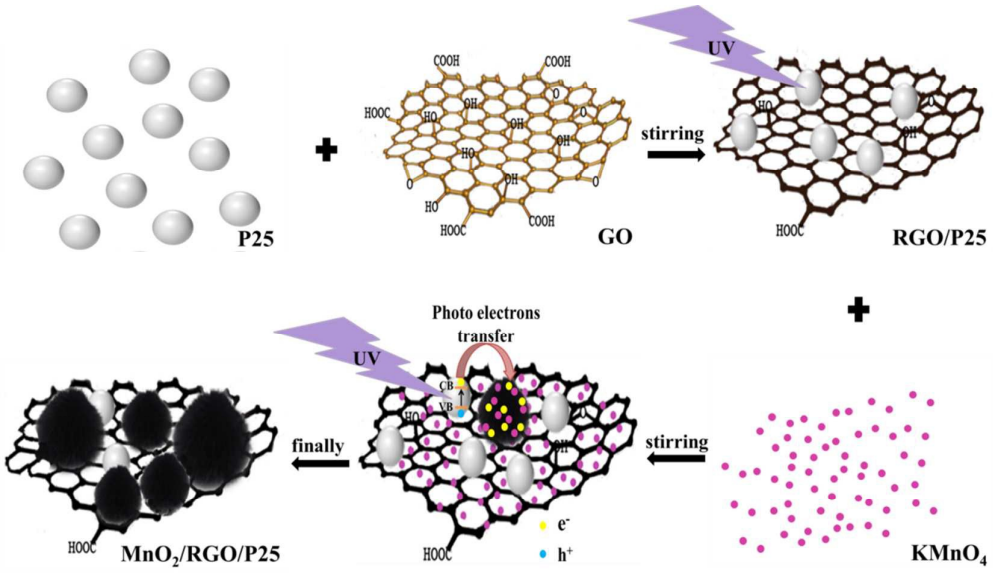

Scheme 1. Photo-reduction synthesis of MnO_2/RGO/P25 nanocomposites.

3. Results and discussion

3.1 Photo-reduction synthesis of MnO_2/RGO/P25 nanocomposites.

As shown in Scheme 1, when P25 was first irradiated with UV lights, the electrons would be excited from the valence bands to the conduction bands, leaving holes in valence bands and generating photo electron-hole pairs in this process (Eqs. 1). Then, the photo holes reacted with H_2O to generate oxygen and GO was photo-reduced to RGO with photo electrons (Eqs. 2 and 3). Lastly, $KMnO_4$ solution was drop-wise added into RGO/P25 homogenous dispersion solution irradiated with UV light to synthetize MnO_2/RGO/P25 nanocomposites (Eqs. 4). The photo-assisted reduction mechanism might be proposed as follows [34, 39−43]:

$$P25 + h\nu \rightarrow P25\ (3h^+) + P25\ (3e^-) \quad (1)$$

$$P25\ (3h^+) + \frac{3}{2}H_2O \rightarrow P25 + \frac{3}{4}O_2 + 3H^+ \quad (2)$$

$$P25\ (3e^-) + GO \rightarrow RGO/P25 \quad (3)$$

$$RGO\ (3e^-)/P25 + MnO_4^- + 4H^+ \rightarrow MnO_2/RGO/P25 + 2H_2O \quad (4)$$

3.2 Field emission scanning electron microscopy (FESEM)

Morphologies of GO, RGO/P25 and MnO_2/RGO/P25 were characterized by FESEM. As shown in Fig.1A, GO displays a tentative structure with affluent wrinkles. From the image of RGO/P25 nanocomposites (Fig.1B), P25 nanoparticles with diameter in the range of 20−30 nm were wrapped by RGO and attached on the surface of photo-reduced graphene oxide sheets. Fig.1C shows MnO_2/RGO/P25 nanocomposites were formed after MnO_4^- ions were photo-reduced and anchored on the surface of RGO/P25. RGO/P25 is likely to provide the nucleation sites for growing preferably to form MnO_2 nanoplatelets.

Most of MnO_2 nanoparticles have a size of ~100 nm and disperse on the surface of RGO/P25 nanocomposites. Fig.1D, 1E and 1F correspond to real samples of GO, RGO/P25 and MnO_2/RGO/P25 composites, respectively. Obviously, the colors of GO, RGO/P25 and MnO_2/ RGO/P25 visibly change from brownish to black after irradiation.

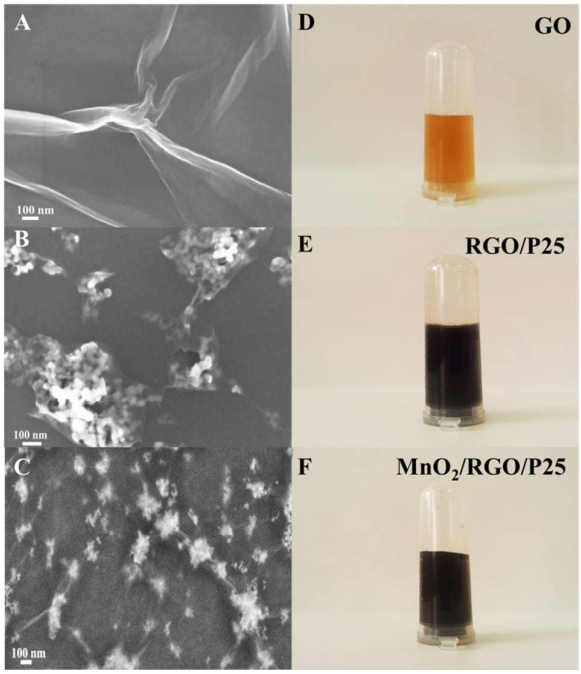

Fig. 1. FESEM images of GO (A), RGO/P25 (B) and MnO_2/RGO/P25(C); photos of GO (D), RGO/P25 (E) and MnO_2/RGO/P25 (F).

3.3 X-ray photoelectron spectroscopy

The surface chemical states of GO, RGO/GO, MnO_2/RGO/P25 were examined by XPS. Fig 2A shows the XPS of MnO_2/RGO/P25. Different C1s binding energies imply the existence of different chemical environments of carbon in GO (Fig. 2B), RGO/GO (Fig. 2C), MnO_2/RGO/P25 (Fig. 2D). As shown in spectra, four peaks with binding energies of 284.8, 286.7, 287.4 and 288.9 eV, can be assigned to the contributions of the C−C (sp^2) bonds, C−O bonds, C=O bonds

and O=C−O bonds [44], respectively. Compared to GO, peak intensity at 284.8 eV in RGO/GO and MnO_2/RGO/P25 increased after illumination, indicating GO were reduced into RGO. Fig. 2E shows the Mn 2p XPS of MnO_2/RGO/P25. The peaks observed at 641.9 and 653.7 eV with a BE difference of 11.8 eV were ascribed to Mn $2p^{3/2}$ and Mn $2p^{1/2}$, respectively [45]. These results agree well with Mn (IV) characters in phase of MnO_2.

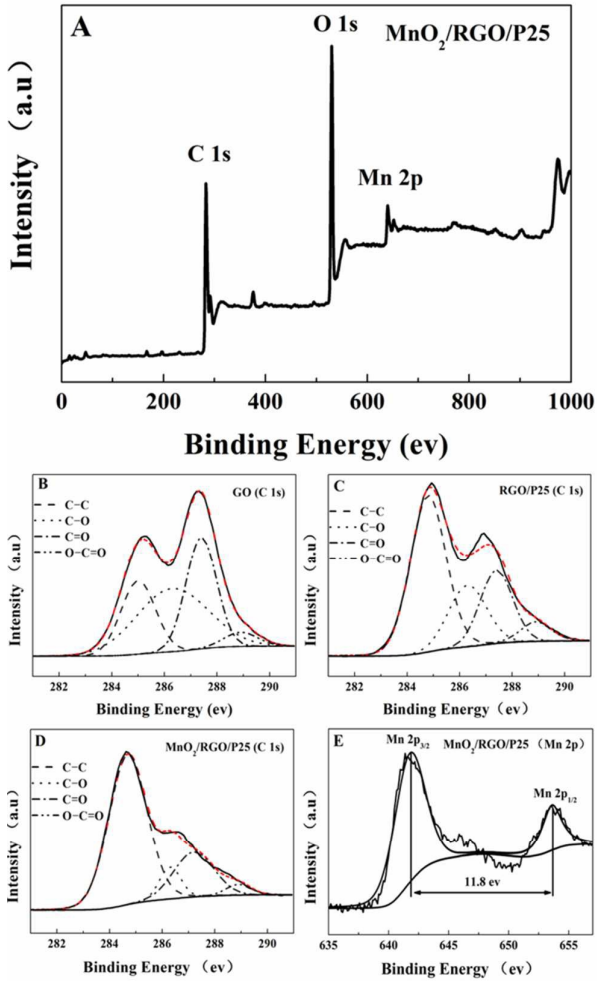

Fig. 2 XPS of MnO_2/RGO/P25 nanocomposites (A); C1s XPS spectra of GO (B), RGO/P25 (C) and MnO_2/RGO/P25 nanocomposites (D); Mn2p XPS spectra of MnO_2/RGO/P25 nanocomposites (E).

3.4 Raman and FTIR spectroscopy

Samples of GO, RGO/P25 and MnO_2/RGO/P25 were also characterized by

Raman spectroscopy recorded between 100 and 2000 cm^{-1} at the same laser power and acquisition time. As depicted in Fig. 3A, GO shows two broadened characteristic frequencies at 1344 and 1597 cm^{-1} corresponding to the D and G bands, respectively [46−47]. Higher intensity ratio means higher defects in GO comprising less sp^2 hybridization. The intensity ratio of D and G bands (I_D/I_G) of GO is 1.06. After photo-reduction reaction process, this value decreases to 1.03 in RGO/P25 and 1.02 in MnO_2/RGO/P25 indicating more graphitization of GO. Compared MnO_2/RGO/P25 with RGO/P25, there is no significant change of the I_D/I_G value after further UV-light irradiation, which indicates no obvious sp^2 hybridization after further photo-reduction reaction [48]. Raman results are also in agreement with the X-ray photoelectron spectra in Fig. 2. Raman spectra of RGO/P25 and MnO_2/RGO/P25 further show frequencies at 398 and 507 cm^{-1} ascribing to the B_{1g} and A_{1g} vibrational modes of TiO_2 anatase phase, respectively. The presence of rutile phase is characterized by peaks at 153 and 630 cm^{-1} which correspond to the modes B_{1g} and A_{1g}. The band at 680 cm^{-1} of MnO_2/RGO/P25 is always seen in MnO_2 materials and corresponds to the symmetric stretching vibration (Mn−O) of the octahedral [MnO_6] groups [49] indicating that MnO_2 were introduced. The red shift in the G band from 1597 to 1591 cm^{-1} is possibly due to increased numbers of isolated carbon double bonds in disordered GO after photo-reduction reaction.

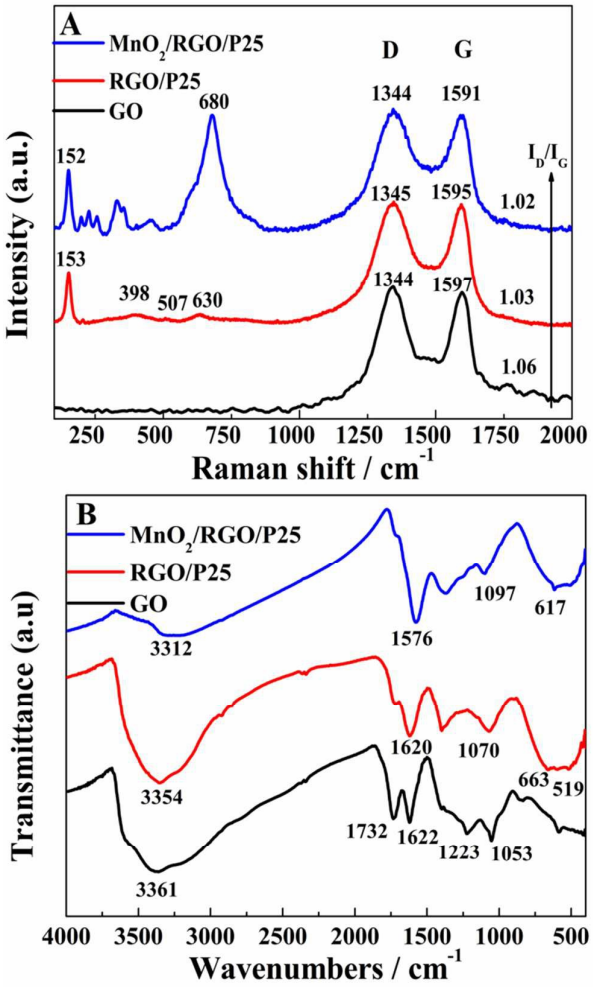

Fig. 3 Raman spectra of GO, RGO/P25 and MnO_2/RGO/P25 (A); FTIR spectra of GO, RGO/P25 and MnO_2/RGO/P25 (B).

FTIR spectra of GO, RGO/P25 and MnO_2/RGO/P25 nanocomposites were recorded in 400-4000 cm^{-1}. As shown in Fig. 3B, all samples present a broad absorption peaks around 3300 cm^{-1}, which are attributed to the surface absorbed water [50]. In the FTIR spectrum of GO, the absorption peaks at 1732 and 1622 cm^{-1} correspond to the C=O stretching and C=C stretching vibrations, respectively (curve a). The band at 1223 cm^{-1} can be ascribed to the epoxy groups vibrations of GO. Compared to GO, the peaks at 1732 and 1223 cm^{-1} of RGO/P25 and MnO_2/RGO/P25 nanocomposites disappeared, which indicate reduction of GO and

its transformation into RGO (curve b and c). The peak appearing at 1053, 1070 and 1093 cm^{-1} are assigned to the vibrations of C–O in alkoxy of GO (curve a), RGO/P25 (curve b) and MnO_2/RGO/P25 (curve c), respectively. For RGO/P25 nanocomposites, the broad absorption at low frequency of 663 cm^{-1} and 519 cm^{-1} (below 1000 cm^{-1}) are attributed to the vibration of Ti–O–Ti bonds in P25. FTIR spectrums of MnO_2/RGO/P25 nanocomposites also show two peaks at 617 and 509 cm^{-1} corresponding to the stretching vibrations of Mn–O–Mn and Mn–O bonds, respectively.

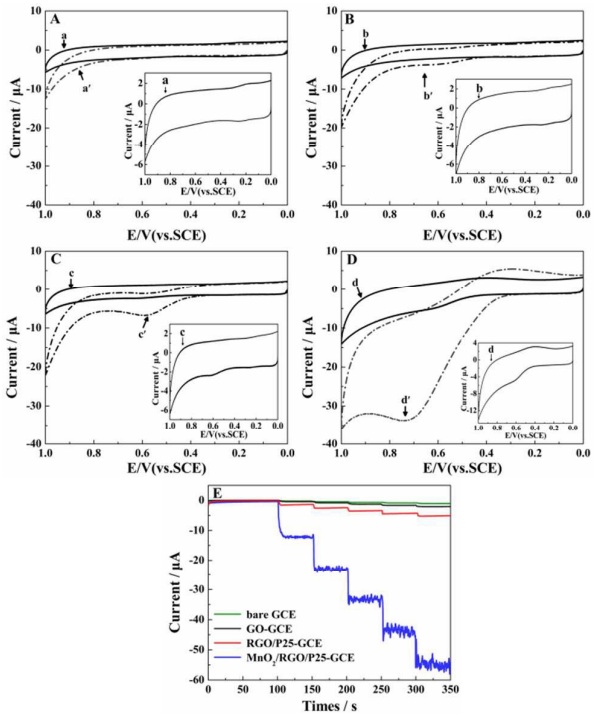

Fig. 4 Cyclic voltammograms of bare GCE (A), GO-GCE (B), RGO/P25-GCE (C) and MnO_2/RGO/P25-GCE (D) in the absence (curve a, b, c and d) and presence (curve a', b', c' and d') of 1 mM H_2O_2 in 0.1 M PBS (pH 8) at scan rate of 100 mV s^{-1}; Amperometric response of bare GCE, GO-GCE, RGO/P25-GCE and MnO_2/RGO/P25-GCE on a successive of 0.5 mM H_2O_2 added into 0.1 M PBS (pH 8) with applied potential of +0.6 V (E). Insets: The amplified cyclic voltammogram of GCE (a), GO-GCE (b), RGO/P25-GCE (c) and MnO_2/RGO/P25-GCE (d) in the absence (curve c) of 1 mM H_2O_2 in 0.1 M PBS (pH 8).

3.5 Electrochemical behavior of MnO_2/RGO/P25 modified glassy carbon electrode

In order to evaluate the electrocatalytic properties of MnO_2/RGO/P25 to oxidation of H_2O_2, the performance of bare GCE, GO-GCE, RGO/P25-GCE and MnO_2/RGO/P25-GCE was evaluated by cyclic voltammetry in 0.1 M PBS (pH 8) at the scan rate of 100 mV s^{-1}. Fig. 4 shows CVs of bare GCE (A), GO-GCE (B), RGO/P25-GCE (C) and MnO_2/RGO/P25-GCE (D) in the absence (curve a, b, c, d) and presence (curve a', b', c' and d') of 1 mM H_2O_2 in 0.1 M PBS (pH 8) at scan rate of 100 mV s^{-1}. . In the absence of H_2O_2, no oxidation peaks were observed at bare GCE (curve a) and GO-GCE (curve b). A very weak oxidation peak around +0.61 V in the absence of 1 mM H_2O_2 in 0.1 M PBS (pH 8) was observed at RGO/P25-GCE (Fig.4C, insert) which might be ascribed to oxidation of RGO [51]. In contrast MnO_2/RGO/P25-GCE (curve d) displayed a pair of broad but weak peaks in the potential range of 0 − 1.0 V in the absence of H_2O_2, which might be attributed to the reduction of MnO_2 to Mn (II or III) and the reoxidation of Mn (II or III) back to MnO_2 [52−53]. When 1mM H_2O_2 was added into 0.1 M PBS (pH 8), no obvious electrochemical oxidation peaks were observed at bare GCE (curve a') and GO-GCE (curve b'). A weak electrochemical oxidation peak was observed at RGO/P25-GCE (curve c'). Compared with bare GCE (curve a'), GO-GCE (curve b') and RGO/P25-GCE (curve c'), a broad and strong oxidation peak was observed on MnO_2/RGO/P25-GCE (curve d') at around +0.7 V in 0.1 mM H_2O_2 + 0.1 M PBS (pH 8). Considering the standard potential values of Mn species, we can make a

conclusion that reductive peaks and oxidative peaks are assigned to the reduction of MnO_2 to Mn (II, III) (Eqs. 5 and 6) and the oxidation of Mn (II, III) to Mn (IV) (Eqs. 7 and 8) [52−53], respectively. The electrochemical reaction mechanism is proposed as following equations:

$$2MnO_2/RGO/P25\ (s) + H_2O_2\ (aq) \rightarrow Mn_2O_3/RGO/P25\ (s) + O_2\ (g) + H_2O \quad (5)$$

$$MnO_2/RGO/P25\ (s) + H_2O_2\ (aq) \rightarrow Mn(OH)_2/RGO/P25\ (s) + O_2\ (g) \quad (6)$$

$$Mn_2O_3/RGO/P25(s) + 2OH^-\ (aq) \rightarrow 2MnO_2/RGO/P25\ (s) + H_2O\ (l) + 2e^- \quad (7)$$

$$Mn(OH)_2/RGO/P25(s) + 2OH^-\ (aq) \rightarrow MnO_2/RGO/P25\ (s) + 2H_2O\ (l) + 2e^- \quad (8)$$

The amperometric response of bare GCE, GO-GCE, RGO/P25-GCE and MnO_2/RGO/P25-GCE toward a successive of 0.5 mM H_2O_2 were also investigated in 0.1 M PBS (pH 8) with applied potential of +0.6 V, as shown in Fig. 4E. MnO_2/RGO/P25 nanocomposites modified GCE exhibited highest sensitivity.

3.6 Optimization of experimental parameters

The content of MnO_2 is a key factor to influence the response current. The influence of $KMnO_4$ was investigated using amperometric response to 0.5 mM H_2O_2 in 0.1 M PBS (pH 8) at the scan rate of 100 mV s^{-1}. As shown in Fig. 5A, the response current of H_2O_2 increased with increase of $KMnO_4$ from 0 to 0.6 mg. However, the response current decreased with further increase of $KMnO_4$. At first, a large number of MnO_2 can be easily anchored on the surfaces of RGO, which provide more electrocatalytic sites and significantly increase the response current towards H_2O_2. However, further increases of $KMnO_4$ result in the agglomeration

of MnO_2, which decrease conductivity of MnO_2/RGO/P25 and slows mass transport through the electrode surface [54].

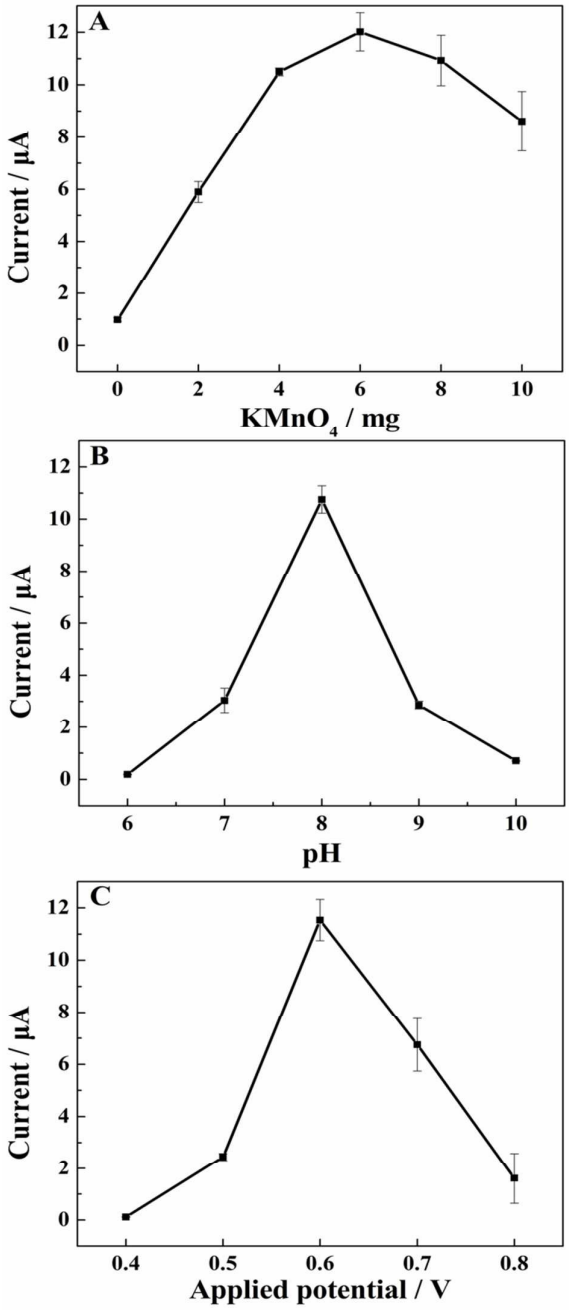

Fig. 5 Effects of $KMnO_4$ (A) and applied potential (C) on the amperometric response of 0.5 mM H_2O_2 in 0.1 M PBS (pH 8) at scan rate of 100 mV s^{-1} with applied potential of +0.6 V; Effects of different pH value on the amperometric response of 0.5 mM H_2O_2 in 0.1 M PBS (pH 8) at scan rate of 100 mV s^{-1} (B). Error bars represent the standard deviation for three independent measurements.

The pH value of the electrolyte is also a crucial parameter affecting the stability and activity of the modified electrode. In order to obtain optimal amperometric response to H_2O_2, different pH values on the amperometric response of 0.5 mM H_2O_2 in 0.1 M PBS were also tested with the applied potential of +0.6 V at the scan rate of 100 mV s^{-1}(B). The response current of H_2O_2 rose strikingly upon the increase of pH 6 − 8 and reached the maximum for pH 8, and then sharply decreased. Thus, pH 8 was chosen as the optimal pH for amperometric H_2O_2 sensing.

It is well known that the applied potential strongly affects the amperometric responses. The influence of the applied potential of the electrocatalytic activity of MnO_2/RGO/P25-GCE was investigated using amperometric response to 0.5 mM H_2O_2 in 0.1 M PBS (pH 8) at the scan rate of 100 mV s^{-1}. The response current increased sharply with the increase of applied potential until the potential reached +0.6 V. The response current drastically decreased when the applied potential exceeded +0.6 V. Therefore, +0.6 V was selected for the amperometric detection of H_2O_2.

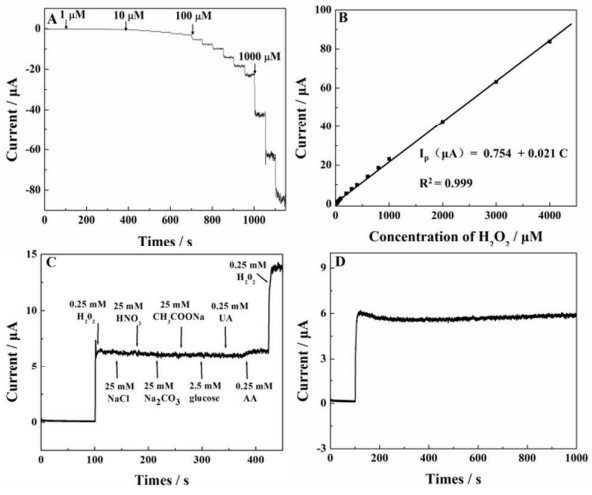

Fig. 6 Amperometric response of MnO_2/RGO/P25-GCE of different concentrations of H_2O_2 in 0.1 M PBS (pH 8) at applied potential of +0.6 V (A); Corresponding calibration curve of MnO_2/RGO/P25-GCE (B); Amperometric response of MnO_2/RGO/P25-GCE to 0.25 mM H_2O_2 and different interferences in stirring 0.1 M PBS (pH 8) with applied potential at +0.6 V (C); The current change of MnO_2/RGO/P25-GCE to 0.25 mM H_2O_2 during 1000 s test period in 0.1 M PBS (pH 8) with applied potential at +0.6 V (D).

3.7 Linearity, selectivity and stability

Under the optimum conditions, MnO_2/RGO/P25-GCE exhibited high rapid and sensitive response for H_2O_2 as displayed in Fig. 6A. The current response is linear with H_2O_2 concentration in the range of 1−4000 μM with sensitivity of 297.2 μA mM^{-1} cm^{-2}, as shown in Fig. 6B. The corresponding regression equation is I (μA) = 0.754 + 0.021 C (μM) (R^2=0.999). The detection limit is estimated to be 0.3 μM (S/N=3). Selectivity is also an important aspect for sensors. The interferences of various common interfering substances including 100-fold concentration inorganic species such as CO_3^{2-}, NO_3^-, CH_3COO^-, Cl^-, K^+ and Na^+ and organic species ascorbic acid (AA, 1-fold), uric acid (UA, 1-fold) and glucose (10-fold) were evaluated towards H_2O_2 analysis. The interferences with the amperometric determination of 0.25 mM H_2O_2 was implemented under optimal conditions in 0.1 M PBS (pH 8), as shown in Fig. 6C. The results show that all interfering agents had response currents are less than 4% of that produced by H_2O_2, indicating high selectivity of MnO_2/RGO/P25-GCE for detecting H_2O_2. We also used the amperometric response method to evaluate the stability of MnO_2/RGO/P25-GCE at +0.6 V in 0.1M PBS (pH 8). As shown in Fig. 6D, the respond current change a little during 1000 s test period indicating that MnO_2/RGO/P25-GCE shows high stability.

Table 1 Performance comparison of the proposed MnO_2/RGO/P25-GCE with other glucose sensors.

Modified electrode	Linear range (μM)	Detection limit (μM)	Sensitivity (μA mM^{-1} cm^{-2})	Reference
Mn-NTA[a]/Nafion	5−2500	0.2	78.9	[9]
MnO_2 nanorods	—	5±2.5	—	[53]
GO/MnO_2	5−600	0.8	38.2	[55]
MnO_2/VACNTs[b]	1.2−1800	0.8	1080	[56]
MnO_2/CF[c]	2.5−2055	0.12	54	[57]
MnO_2/graphene/CNT[d]	1−1030	0.1	539.4	[58]
MnO_2/RGO/P25	1−4000	0.3	297.2	This work

[a] NTA stands for nitrilotriacetateacid;
[b] VACNTs stands for vertically aligned multiwalled carbon nanotubes;
[c] CF stands for carbon foam;
[d] CNT stands for graphene/carbon nanotubes.

Table 2 Determination of H_2O_2 in toothpaste samples (n=3).

Toothpaste samples	Detected (μM)	Added (μM)	Founded (μM)	Recovery (%)	RSD (%)
1	18.24	20.00	38.38	100.3	2.9
2	20.05	20.00	38.81	96.7	4.7
3	17.95	20.00	37.10	97.8	3.4

3.8 Real sample analysis

The application for real sample analysis of MnO_2/RGO/P25-GCE was evaluated by the determination of H_2O_2 in toothpaste. Briefly, 1.0 g toothpaste mixed with 10 ml PBS (0.1 M pH 8) was centrifuged before test. H_2O_2 has been estimated directly by amperometric method under optimal conditions with standard addition method. The detection result is shown in Table 2. The results have demonstrated that MnO_2/RGO/P25 has potential applications in the determination of H_2O_2 in real samples.

4. Conclusion

In this work, a non-enzymatic H_2O_2 sensor based on MnO_2/RGO/P25

nanocomposites has been successfully prepared using a novel photo-reduction assisted synthesis method. The as-prepared sensor exhibited highly electrocatalytic activity, selectivity and stability towards the oxidation of H_2O_2. Under optimum conditions, the calibration curve for H_2O_2 determination was linear in the range from 1.0×10^{-6} to 4.0×10^{-3} M ($R^2 = 0.999$) with a detection limit of 3×10^{-7} M (S/N = 3). The proposed synthesis method is mild and simple, and the synthesized MnO_2/RGO/P25 nanocomposites possess low toxicity. The present study provides a novel approach for the construction of non-enzyme sensors.

Acknowledgments

This research is supported by the National Natural Science Foundation of China (Nos. 61171033, 61571278, 61571280).

References

1. S. wolfbeis, A. Dürkop, M. Wu and Z. H. Lin, *Angew Chem Int Edit*, 2002, **41**, 4495−4498.
2. E. C. Hurdis and H. Romeyn, *Anal Chem*, 1954, **26**, 320−325.
3. B. X. Li, Z. J. Zhang and Y. Jin, *Sensor Actuat B Chem*, 2001, **72**, 115−119.
4. H. Cui, W. Wang, C. F. Duan, Y. P. Dong and J. Z. Guo, *Chem Eur J*, 2007, **13**, 6975−6984.
5. Y. Z. Li and A. Townshend, *Anal Chim Acta*, 1998, **359**, 149−156.
6. K. Sunil and B. Narayana, *B Environ Contam Tox*, 2008, **81**, 422−426.
7. S. Y. Xu, B. Peng and X. Z. Han, *Biosens Bioelectron*, 2007, **22**, 1807−1810.
8. Q. Rui, K. K. Komori, Y. Tian, H. Q. Liu, Y. P. Luo and Y. Sakai, *Anal Chim*

Acta, 2010, **670**, 57−62.

9. S. Liu, L. M. Li, Q.Y. Hao, X. M. Yin, M. Zhang, Q. H. Li, L. B. Chen and T. H. Wang, *Talanta*, 2010, **81**, 727−731.
10. X. B. Lu, J. H. Zhou, W. Lu, Q. Liu and J. H. Li, *Biosens Bioelectron*, 2008, **23**, 1236−1243.
11. C. H. Wang, C. Yang, Y. Y. Song, W. Gao and X. H. Xia, *Adv Funct Mater*, 2005, **15**, 1267−1275.
12. L. Zhang, *Biosens Bioelectron*, 2008, **23**, 1610−1615.
13. L. M. Li, Z. F. Du, S. Liu, Q. Y. Hao, Y. G. Wang, Q. H. Li and T. H. Wang, *Talanta*, 2010, **82**, 1637−1641.
14. H. Yao, H. Liu, M. Sun and L. Gong, *Microchim Acta*, 2012, **177**, 31−37.
15. J. Narang , N. Chauhan and C.S. Pundir, *Analyst*, 2011, **136**, 4460−4466.
16. S. Gupta and R. Prakash, *J Mater Chem C*, 2014, **2**, 6859−6866.
17. S. Gupta and R. Prakash, *RSC Adv*, 2015, **5**, 81660−81667.
18. S. S. Kumar, J. Joseph and K. L. Phani, *Chem Mater*, 2007, **19**, 4722−4730.
19. W. Li, L. Kuai, Q. Qin and B. Geng, *J. Mater. Chem. A*, 2013, **1**, 7111−7117.
20. G. S. Cao, P. Wang, X. Li, Y. Wang, G. Wang and J. Li, *Nano Lett*, 2014, **9**, 16−18.
21. D. Chen, H. Feng and J. Li, *Chem. Rev*, 2012, **112**, 6027−6053.
22. K. L. Wu, X. Z. Li, C. Dong, L. Liu, P. D. Liu, T. H. Ding, J. Lu and X. W. Wei, *Chem. Lett*, 2013, **42**, 1466−1468.
23. X. Zhang, J. Zhang, D. Zhou and G. Wang, *Micro Nano Lett*, 2012, **7**, 60−63.

24. D. X. Ye, H. X. Li, G. H. Liang, J. Luo, X. X. Zhang, S. Zhang, H. Chen and J. L. Kong, *Electrochim Acta*, 2013, **109**, 195−200.

25. F. Xiao, Y. Q. Li, X. L. Zan, K. Liao, R. Xu and H. W. Duan, *Adv Funct Mater*, 2012, **22**, 2487−2494.

26. J. Y Lei, X. F Lu, W. Wang, X. J. Bian, Y. P. Xue, C. Wang and L. J. Li, *RSC Adv*, 2012, **2**, 2541−2544.

27. K. I. Bolotin, K. J. Sikes, Z. Jiang, M. Klima, G. Fudenberg, J. Hone, P. Kim and H. L. Stormer, *Solid State Commun*, 2008, **146**, 351−355.

28. A. A. Balandin, S. Ghosh, W. Z. Bao, I. Calizo, D. Teweldebrhan, F. Miao and C. N. Lau, *Nano Lett*, 2008, **8**, 902−907.

29. M. J. McAllister, J. L. Li, D. H. Adamson, H. C. Schniepp, A. A. Abdala, J. Liu, H. A. Margarita, D. L. Milius, R. Car, R. K. Prud'homme and I. A. Aksay, *Chem Mater*, 2007, **19**, 4396−4404.

30. S. Stankovich, D. A. Dikin, G. H. Dommett, K. M. Kohlhaas, E. J. Zimney, E. A. Stach, R. D. Piner, S. T. Nguyen and R. S. Ruoff, *Nature*, 2006, **442**, 282−286.

31. X. Wang, L. J. Zhi and K. Müllen, *Nano Lett*, 2008, **8**, 323−327.

32. Y. Zhou, Q. L. Bao, B. Varghese, L. Ai, L. Tang, C. K. Tan, C. H. Sow and K. P. Loh, *Adv Mater*, 2010, **22**, 67−71.

33. C. Liu, Y. Teng, R. Liu, S. Luo, Y. Tang, L. Chen and Q. Cai, Carbon, 2011, **49**, 5312–5320.

34. B. Li, X. T. Zhang, X. H. Li, L. Wang, R. Y. Han, B. B. Liu, W. T. Zheng, X. L.

Li and Y. C. Liu, *Chem Commun*, 2010, **46**, 3499−3501.

35. S. Kalathil, M. M. Khan, S. A. Ansari, J. Lee and M. H. Cho, *Nanoscale*, 2013, **5**, 6323−6326.
36. M. M. Khan, S. A. Ansari, M. I. Amal, J. Lee and M. H. Cho, *Nanoscale*, 2013, **5**, 4427−4435.
37. H. Ishiguro, R. Nakano, Y. Y. Yao, J. Kajioka, A. Fujishima, K. Sunada, M. Minoshima, K. Hashimotod and Y. Kubota, *Photoch Photobio Sci*, 2011, **10**, 1825−1829.
38. M. A. Zwijnenburg, S. T. Bromley, J. C. Jansen and T. Maschmeyer, *Chem Mater*, 2004, **16**, 12−20.
39. A. Fujishima and K. Honda, *Nature*, 1972, **238**, 37–38.
40. G. Williams, B. Seger and P. V. Kamat, *ACS Nano*, 2008, **2**, 1487−1491.
41. A. Ajmal, I. Majeed, R. N. Malik, H. Idrissc and M. A. Nadeem, *RSC Adv*, 2014, **4**, 37003–37026.
42. Y. Y. Zhu, Y. J. Wang, W. Q. Yao, R. L. Zong and Y. F. Zhu, *RSC Adv*, 2015, **5**, 29201–29208.
43. Y. L. Liu, K. Q. Chen, M. Y. Xiong, P. Zhou, Z.Y. Peng, G. J. Yang, Y. Q. Cheng, R. B. Wang and W. Chen, *RSC Adv*, 2014, **4**, 43760–43765.
44. H. K. Jeong, Y. P. Lee, R. J. Lahaye, M. H. Park, M. H. An, I. J. Kim, C. W. Yang, C. Y. Park, R. S. Ruoff and Y. H. Lee, *J Am Chem Soc*, 2008, **130**, 1362−1366.
45. C. D. Wanger, W. M. Riggs, L. E. Davis, J. F. Moulder and G. E. Muilenberg,

Handbook of x-ray photoelectron spectroscopy, Perkin-Elmer Corp., Physical Electronics Division, Eden Prairie, Minnesota, USA, 1979.

46. K. N. Kudin, B. Ozbas, H. C. Schniepp, R. K. Prudhomme, I. A. Aksay and R. Car, *Nano Lett*, 2008, **8**, 36−41.

47. A. C. Ferrari, J. C. Meyer, V. Scardaci, C. Casiraghi, M. Lazzeri, F. Mauri, S. Piscanec, D. Jiang, K. S. Novoselov, S. Roth and A. K. Geim, *Phys Rev Lett*, 2006, **97**, 187401.

48. Y. H. Zhang, Z. Tang, X. Z. Fu and Y. J. Xu, *ACS Nano*, 2011, **5**, 7426–7435.

49. C. Julien, M. Massot, S. Rangan, M. Lemal and D. Guyomard, *J. Raman Spectrosc*, 2002, **33**, 223–228.

50. G. S. Shao, X. J. Zhang and Z. Y. Yuan, *Appl Catal B-environ*, 2008, **82**, 208−218.

51. H. H Wang, Y. Bu, W. L. Dai, K. Li, H. D. Wang, X. Zuo, *Sensor Actuat B Chem,* 2015, **216**, 298–306

52. Y. H. Bai, Y. Du, J. J. Xu and H. Y. Chen, *Electrochem Commun*, 2007, **9**, 2611−2616.

53. B. Xu, M. L. Ye, Y. X. Yu and We. D. Zhang, Analytica Chimica Acta, 2010, **674**, 20−26.

54. S. X. Deng, D. Sun, C. H. Wu, H. Wang, J. B. Liu, Y. X Sun and H. Yan, *Electrochim Acta*, 2013, **111**, 707−712.

55. L. M. Li, Z. F. Du, S. Liu, Q. Y. Hao, Y. G. Wang, Q. H. Li and T. H. Wang, *Talanta*, 2010, **82**, 1637−1641.

56. B. Xu, M. L. Ye, Y. X. Yu and W. D. Zhang, *Anal Chim Acta*, 2010, **674**, 20−26.

57. S. J. He, B. Y. Zhang, M. M. Liu and W. Chen, *RSC Adv*, 2014, **4**, 49315−49323.

58. D. X. Ye, H. X. Li, G. H. Liang, J. Luo, X. X. Zhang, S. Zhang, H. Chen and J. L. Kong, *Electrochim Acta*, 2013, **109**, 195−200.

Graphical Abstract:

MnO_2/RGO/P25 nanocomposites were synthesized with photo-reduction approach for electrochemical detection of H_2O_2.